

# MRI-driven Accretion on to Magnetized stars: Global 3D MHD Simulations of Magnetospheric and Boundary Layer Regimes

M. M. Romanova,<sup>1\*</sup>, G. V. Ustyugova,<sup>2</sup>, A. V. Koldoba<sup>2</sup>, R. V. E. Lovelace<sup>1</sup>

<sup>1</sup> Department of Astronomy, Cornell University, Ithaca, NY 14853-6801, USA

<sup>2</sup> Keldysh Institute for Applied Mathematics, Moscow, Russia

4 November 2018

## ABSTRACT

We discuss results of global three-dimensional (3D) magnetohydrodynamic (MHD) simulations of accretion on to a rotating magnetized star with a tilted dipole magnetic field, where the accretion is driven by the *magneto-rotational instability* (MRI). The simulations show that MRI-driven turbulence develops in the disc, and angular momentum is transported outwards due primarily to the magnetic stress. The turbulent flow is strongly inhomogeneous and the densest matter is in azimuthally-stretched turbulent cells. We investigate two regimes of accretion: a magnetospheric regime and a boundary layer (BL) regime. In the magnetospheric regime, the magnetic field of the star is dynamically important: the accretion disc is truncated by the star’s magnetic field within a few stellar radii from the star’s surface, and matter flows to the star in funnel streams. The funnel streams flow towards the south and north magnetic poles but are not equal due to the inhomogeneity of the flow. The hot spots on the stellar surface are not symmetric as well. In the BL regime, the magnetic field of the star is dynamically unimportant, and matter accretes to the surface of the star through the boundary layer. The magnetic field in the inner disc is strongly amplified by the shear of the accretion flow, and the matter and magnetic stresses become comparable. Accreting matter forms a belt-shaped hot region on the surface of the star. The belt has inhomogeneous density distribution which varies in time due to variable accretion rate. The peaks in the variability curve are associated with accretion of individual turbulent cells. They show 20-50% density amplifications at periods  $\sim 5 - 10$  dynamical time-scales at the surface of the star. Spiral waves in the disc are excited in both, magnetospheric and boundary layer regimes of accretion. Results of simulations can be applied to classical T Tauri stars, accreting brown dwarfs, millisecond pulsars, dwarf novae cataclysmic variables, and other stars with magnetospheres smaller than several stellar radii.

## 1 INTRODUCTION

Different types of stars have *dynamically important* magnetic fields. These include young, classical T Tauri stars (hereafter - CTTS; e.g., Bouvier, et al. 2007), young accreting brown dwarfs (e.g., Mohanty et al. 2005), accreting neutron stars (e.g., Lewin et al. 1995; Van der Klis 2000), and different types of cataclysmic variables, including dwarf novae and intermediate polars (e.g., Hellier 2001; Warner 2003). In such stars, the accretion disc is truncated at the disc-magnetosphere boundary, and the magnetic field governs the matter flow (e.g., Pringle & Rees 1972; Ghosh & Lamb 1979; Königl 1991; Collier Cameron & Campbell 1993; Wang 1995; Campbell 2010). We refer to this regime as the *magnetospheric regime* of accretion. On the other hand, many accreting neutron stars, white dwarfs, and other stars are expected to have relatively weak, *dynamically-unimportant* magnetic field, and accrete in the equatorial region of the star in the

*boundary layer regime* (e.g., Popham & Narayan 1995; Inogamov & Sunyaev 1999; Piro & Bildsten 2004; Fisker & Balsara 2005).

The physics of the disc-magnetosphere interaction depends on both the properties of the magnetized star and the properties of the accretion disc. Accretion in the disc can be smooth as modelled by including an  $\alpha$ -viscosity (Shakura & Sunyaev 1973) in the MHD equations. Or, it can be strongly turbulent owing to the growth of the magneto-rotational instability (Velikhov 1959; Chandrasekhar 1960; Balbus & Hawley 1991, 1998).

Interaction of a magnetized star with  $\alpha$ -type discs has been investigated in a number of axisymmetric simulations (e.g., Miller & Stone 1997; Romanova et al. 2002; Long et al. 2005; Bessolaz et al. 2008), and in global 3D simulations (e.g., Romanova et al. 2003, 2004, 2008; Kulkarni & Romanova 2005, 2008; Long et al. 2007, 2008, 2011). These simulations confirmed many properties of the disc-

arXiv:1111.3068v1 [astro-ph.SR] 13 Nov 2011

magnetosphere interaction predicted by theory. They also revealed new features, connected, for example, with the non-stationarity of the disc-magnetosphere interaction and the possibility of outflows (e.g., Lovelace et al. 1995; Goodson et al. 1997, 1999; Romanova et al. 2005; Ustyugova et al. 2006; Romanova et al. 2009), and possible important role of the interchange instability (Romanova et al. 2008; Kulkarni & Romanova 2008, 2009). Interaction of a magnetized star with a turbulent accretion disc has not been studied as much. MRI-driven turbulence has been extensively studied in axisymmetric and local/global 3D MHD simulations (e.g., Hawley et al. 1995; Brandenburg et al. 1995; Stone et al. 1996; Armitage 1998; Hawley et al. 2001; Stone & Pringle 2001; Beckwith, et al. 2009, 2011; Flock, et al. 2011; Simon et al. 2011). However, in all these simulations, the central object is a *black hole*.

Recently, we performed the first axisymmetric (2.5D) MHD simulations of the MRI-driven accretion on to a *magnetized star* (Romanova et al. 2011a). We observed different phenomena connected with turbulent nature of the disc. However, global 3D simulations are required for more realistic description of MRI-driven turbulence and magnetized stars.

In this paper, we present results from global 3D MHD simulations of MRI-driven, turbulent accretion on to a *magnetized star* with a *tilted* dipole magnetic field. It is necessary to perform the simulations in the full three-dimensional space, including the full range of the azimuthal angle ( $0 - 2\pi$ ). Furthermore, we need to have sufficiently high grid resolution in the disc for the magnetic turbulence to develop and be sustained, and we need to resolve the magnetosphere of the star, which has strong gradients of the dipole magnetic field. Because of these requirements, significant computing time is required, and we performed simulations only during a restricted period of time.

First, we show results of MRI-driven accretion on to stars with dynamically unimportant magnetic field, accreting in the BL regime. In this case, we were able to obtain relatively long runs and investigated MRI-driven accretion in the disc. We also studied the properties of the inner regions of the disc, the disc-star boundary, and variability associated with the turbulence. Next, we show results for the magnetospheric accretion where the disc matter is truncated by the magnetosphere. In this case, we concentrated on the disc-magnetosphere interaction and accretion through the funnel flow.

In §2 we describe the problem setup. In §3 and §4 we show results of simulations for accretion in the boundary layer and magnetospheric regimes, respectively. In §5 we discuss the different stresses in the disc. §6 gives the conclusions from this work.

## 2 PROBLEM SETUP

### 2.1 Magnetosphere and magnetospheric radius

If the magnetic field of the star is relatively strong (in the sense of being dynamically important)<sup>1</sup>, then the accretion disc is truncated by the stellar magnetosphere at some radius  $r_m$ , which is called the *magnetospheric radius*. Different physical arguments were proposed to define this radius (e.g.,

<sup>1</sup> Here, and below in the paper, we use terms ‘strong’ and ‘weak’ for dynamically important and dynamically unimportant fields.

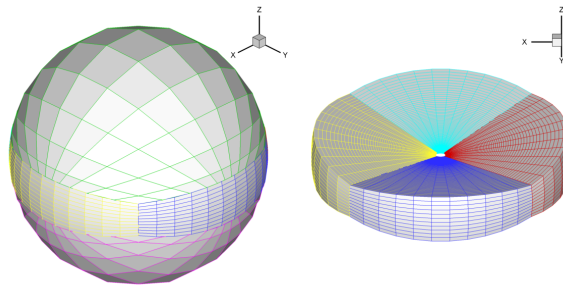


**Figure 1.** The “cubed sphere” grid used in our simulations. The grid is compressed towards the equatorial plane. A low resolution case is shown here to make the grid visible.

Pringle & Rees 1972; Ghosh & Lamb 1979). For example, this radius can be derived from the balance between the magnetic pressure of the magnetosphere and the ram pressure of the accreting matter (e.g., Lamb et al. 1973):  $B^2/8\pi \approx \rho v^2$  (where  $B$  is the local value of the magnetic field,  $\rho$  and  $v$  are density and total velocity in the disc). Then, the magnetospheric radius can be derived in the form, which is often used in theoretical analysis (e.g, Lamb et al. 1973; Königl 1991):

$$r_m = k\mu^{4/7} \dot{M}^{-2/7} GM^{-1/7}, \quad (1)$$

where  $\mu = B_* R_*^3$  is the magnetic moment of the star,  $\dot{M}$  is the accretion rate from the disc, and coefficient  $k \approx 0.5$  (Long et al. 2005).

In simulations, however, we do not know the accretion rate in advance, and it varies with time. Hence, it is better to find the magnetospheric radius directly from the balance of stresses. We introduce

$$\beta_1 = \frac{p + \rho v_\phi^2}{B^2/8\pi}, \quad \beta = \frac{p}{B^2/8\pi}, \quad (2)$$

where,  $p$  is the gas pressure,  $v_\phi$  is the azimuthal component of the magnetic field. Here,  $\beta$  is the commonly used plasma parameter. The modified plasma parameter  $\beta_1$  takes into account the matter stress associated the plasma flow in the disc and it is often more relevant in astrophysical situations than  $\beta$  parameter (Romanova et al. 2002). In accretion discs, the magnitude flow velocity is approximately the azimuthal velocity,  $v \approx v_\phi$ , and hence the matter stress has also a meaning of the ram pressure, and the condition  $\beta_1 = 1$  can be also interpreted as a balance of total pressure at the disc-star boundary. We observed from simulations that this condition always gives the boundary between the disc and the magnetosphere. We use this condition to find  $r_m$  from simulations. Typically we have  $\beta \approx 1$  at radii larger than  $r_m$ , which often shows the place where the funnel streams start flowing from the disc to the star (see also Bessolaz et al. 2008; Campbell 2010).<sup>2</sup>

Modeling of accreting magnetized stars is technically challenging, because in regions of the strongest magnetic field, the matter density is low, and this requires a small time-step in simulations. In  $\alpha$ -type discs, we were able to model relatively large magnetospheres with  $r_m \lesssim 10R_*$  (e.g., Romanova et al. 2006). However, in the current simulations of

<sup>2</sup> Bessolaz et al. (2008) compared several approaches for derivation of  $r_m$  and showed that this radius does not differ much. This is because the magnetic pressure  $\sim B^2 \sim r^{-6}$  is a steep function of  $r$ .

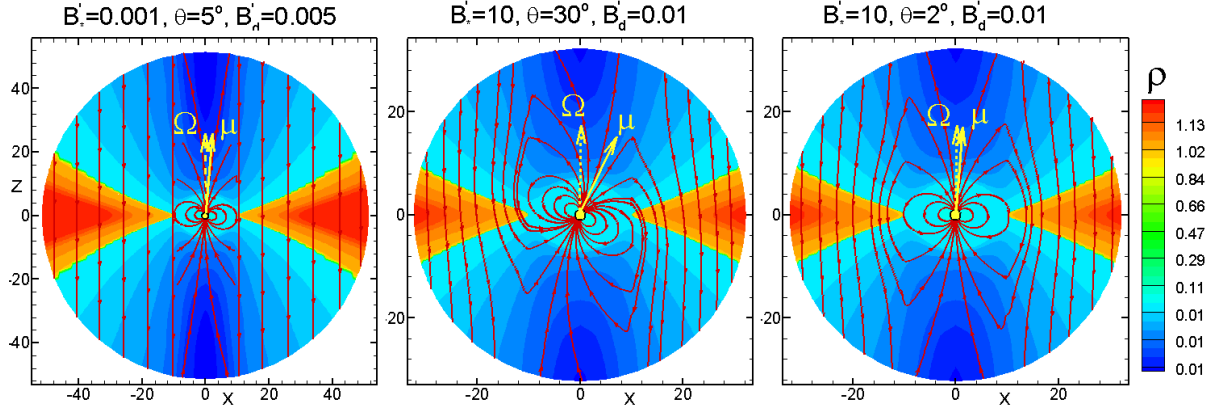


**Figure 2.** The initial distribution of density (color background) and magnetic field lines in the  $xz$ -slice. The left-hand panel shows the case of a dynamically unimportant and slightly tilted stellar magnetic field ( $B'_* = 0.001$ ,  $\Theta = 5^\circ$ ). The two right-hand panels show the cases of a dynamically important stellar magnetic field ( $B'_* = 10$ ) at high ( $\Theta = 30^\circ$ ) and low ( $\Theta = 2^\circ$ ) tilts of the dipole field. The magnetic field in the disc is  $B'_d = 0.005$  and  $B'_d = 0.01$ , respectively.

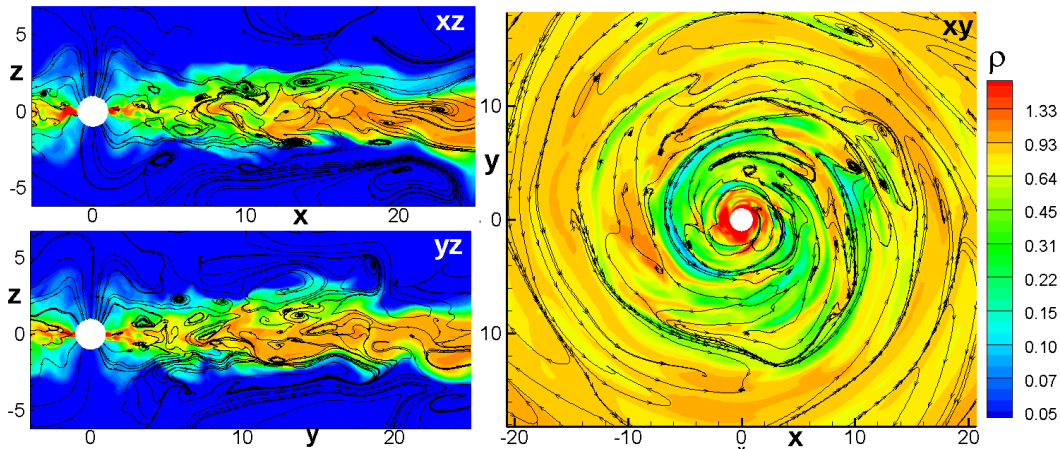


**Figure 3.** Slices of the density distribution (color background) and sample field lines in the case of a star with dynamically unimportant magnetic field ( $B'_d = 0.001$ ,  $\Theta = 5^\circ$ ). The left-hand panels show the  $xz$  and  $yz$  slices, while the right-hand panel shows an equatorial,  $xy$ , slice.

turbulent discs, we model somewhat smaller magnetospheres with  $r_m \approx 3R_*$ , because the duration of simulations strongly increases with the size of the magnetosphere. There are several types of stars where such magnetospheres are expected (e.g., CTTSs, accreting millisecond pulsars, dwarf novae, accreting brown dwarfs, and other stars).

In case of much weaker, dynamically unimportant field, the star's magnetosphere does not truncate the disc. That is, the magnetospheric radius is equal or smaller than the radius of the star,  $r_m \lesssim R_*$ . We use this case for investigation of the MRI-driven accretion in the disc and for analysis of processes at the disc-star boundary in the presence of the magnetic field. These simulations are faster, and they also correspond to an important astrophysical regime of accretion through the boundary layer.

## 2.2 Rotation of the star and corotation radius

Another important parameter of the problem is the corotation radius,  $r_{\text{cor}} = (GM_*/\Omega_*^2)^{1/3}$ , where Keplerian angular velocity in the disc equals the angular velocity of the star,  $\Omega_*$ . The result of the disc-magnetosphere interaction depends on the

ratio between  $r_m$  and  $r_{\text{cor}}$ . In case of slow rotation,  $r_{\text{cor}} \gtrsim r_m$ , the magnetosphere spins the inner parts of the disc down, the gravitational force is larger than the centrifugal force, and accretion is favorable. In the opposite case of rapidly rotating star,  $r_{\text{cor}} < r_m$ , the magnetosphere transfers its angular momentum to the matter of the inner disc, and a star is in the 'propeller' regime, where accretion is suppressed (e.g., Illarionov & Sunyaev 1975; Lovelace et al. 1999; Romanova et al. 2005; Ustyugova et al. 2006). In this paper we consider only the case of slowly rotating stars, which is favorable for accretion. We chose rather large corotation radius,  $r_{\text{cor}} = 10R_*$ , to be sure that we are always in the accretion regime from the beginning of the simulations<sup>3</sup>. The ratio  $r_{\text{cor}}/r_m \approx 3$  is larger than that expected in the rotational equilibrium state<sup>4</sup> where  $r_{\text{cor}} \approx (1.2 - 1.6)r_m$  (the coefficient in front of  $r_m$  depends on parameters of the model (Long et al. 2005)). However, our

<sup>3</sup> Initially, the inner disc radius is located at  $r = 10R_*$ , and this fact determines our choice for  $r_{\text{cor}}$ . Smaller values of  $r_{\text{cor}}$  would be also sufficient.

<sup>4</sup> In the rotational equilibrium state, the torques on the star associated with spinning-up and spinning-down are balanced.

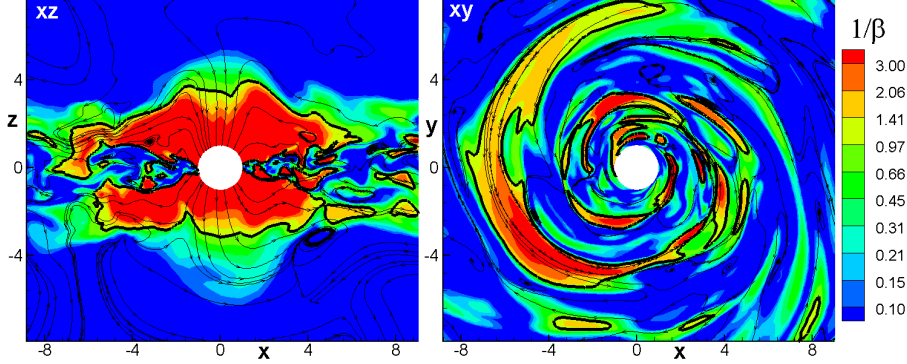


**Figure 4.** The color background shows  $x - z$  (left panel) and  $x - y$  (right panel) slices of the magnetic pressure normalized to matter pressure,  $\beta^{-1} = B^2/8\pi p$ . Thin lines are magnetic field lines, and the bold lines correspond to  $\beta = 1$ .

earlier simulations of  $\alpha$ -discs, performed at different ratios of  $r_m/r_{\text{cor}}$ , show that the result is very similar in cases where  $r_{\text{cor}}$  is larger, or much larger than  $r_m$ . In both cases, the gravitational force dominates and the accretion through the funnel flow has been observed (e.g., Romanova et al. 2002; Long et al. 2005).

### 2.3 MRI-driven turbulence

The turbulence in the disc is initiated and supported by the magneto-rotational instability. Here, we briefly summarize the condition for the onset of this instability (Balbus & Hawley 1991) for a *simple case* where an axial magnetic field  $B_0\hat{z}$  threads a thin Keplerian disc which rotates with angular velocity  $\Omega = (GM_*/r^3)^{1/2}$ . For axisymmetric perturbations of the disc with  $\delta\mathbf{v} = [\delta v_r(z, t), \delta v_\phi(z, t), 0]$  and  $\delta\mathbf{B} = [\delta B_r(z, t), \delta B_\phi(z, t), 0]$  and for perturbations proportional to  $\exp(ik_z z - i\omega t)$ , one finds the dispersion relation

$$\omega_\pm^2 = (k_z v_A)^2 + \frac{1}{2}\kappa_r^2 \pm \left[ \frac{1}{4}\kappa_r^4 + 4(k_z v_A \Omega)^2 \right]^{1/2}, \quad (3)$$

where  $v_A \equiv B_0/\sqrt{4\pi\rho}$  is the Alfvén velocity and  $\kappa_r \equiv [4\Omega^2 + 2r\Omega d\Omega/dr]^{1/2}$  is the radial epicyclic frequency of the disc. In order for the perturbation to fit within the vertical extent of the disc one needs  $k_z h \gtrsim 1$ , where  $h = c_s/\Omega$  is the half-thickness of the disc and  $c_s$  is the midplane isothermal sound speed in the disc.

The instability will develop if  $\omega_-^2 < 0$  which happens if  $(k v_A)^2 < -2r\Omega d\Omega/dr$ . For a Keplerian disc this corresponds to  $(k v_A)^2 < 3\Omega^2$ . Therefore, the above-mentioned condition that  $k_z h \gtrsim 1$  implies that the instability occurs only for  $v_A < c_s$ , or the condition for plasma parameter becomes:

$$\beta = \frac{p}{B_0^2/8\pi} = \frac{2c_s^2}{v_A^2} > 1, \quad (4)$$

where matter pressure  $p = \rho c_s^2$ . Note that  $\beta$  is based on the *initial* vertical magnetic field,  $B_0$ . As a result of the instability the magnetic field may grow to values much larger than  $B_0$ . The maximum value of the growth rate is  $\Im(\omega)_{\text{max}} = 3\Omega/4$ , and it occurs for  $k_{\text{max}} = (15/16)^{1/2}\Omega/v_A$ . For  $\beta < 1$  the perturbation does not fit inside the disc and there is stability. As  $\beta$  increases from unity (weaker magnetic field) the maximum growth rate stays the same but the wavelength of the perturbation gets shorter ( $\propto \beta^{-1/2}$ ). For sufficiently small wavelengths the damping due to numerical viscosity ( $\sim \nu_{\text{num}} k^2$ )

will be larger than the MRI growth rate. To generate MRI-driven accretion in numerical simulations, one should have large enough  $\beta$  in the disc so as to have instability, and at the same time high enough grid resolution to avoid the damping of small wavelengths. This theoretical analysis helps in understanding the initial stages of the MRI instability in our simulations.

### 2.4 Numerical setup

#### 2.4.1 Method and grid

We use three-dimensional (3D) MHD second-order Godunov-type code developed by our group (Koldoba et al. 2002). It has many specific features which are oriented towards efficient calculation of accretion on to a star with a tilted dipole or more complex magnetic fields: (1) the magnetic field  $\mathbf{B}$  is decomposed into the “main” dipole component of the star,  $\mathbf{B}_0$ , and the component  $\mathbf{B}_1$  induced by currents in the disc and the corona (Tanaka 1994); (2) the MHD equations are written in a reference frame which is rotating with the star; and (3) the numerical method uses the “cubed sphere” grid which has the advantages of both the cartesian and spherical coordinate systems and avoids the singularity on the polar axis in the spherical coordinate system. The grid on the surface of the sphere consists of six sectors with the grid in each sector topologically equivalent to the grid on a face of a cube (e.g., Ronchi et al. 1996). In contrast with these authors, we use a Godunov-type numerical scheme similar to the one described by Powell et al. (1999) and perform simulations in the range of azimuthal angles  $(0 - 2\pi)$  in three dimensional space.

In addition, to better resolve the MRI-driven turbulence inside the disc, we compressed the grid towards the equatorial plane (see Fig. 1). This helps to increase the grid resolution in the vertical direction, which is favorable for the investigation of MRI-driven accretion and helps to save computing time. A number of angular grid resolutions has been used:  $N_x = N_y = 51, 61, 71, 81, 91$  (in each of the 6 blocks of the cube). MRI-driven turbulence has been observed in all these cases, and the picture of the accretion flow is qualitatively the same. To save computing time, we use the grid  $N_x = N_y = 61$  as a base. The number of grid cells in the radial direction is  $N_r = 200$  (in the strong field case) and  $N_r = 220$  (in the weak field case), so that the region is 1.6 times larger in the

case of a weak field. The grid compression has been done in such a way that the number of grid cells across the disc in the vertical direction is 80, which is sufficient for resolving the MRI-driven turbulence. The 3D MHD code is parallelized using MPI. We typically use  $N_p = 240 - 360$  processors per run.

#### 2.4.2 Reference Units

3D MHD equations are written in dimensionless form and results can be applicable to a wide variety of stars. We chose mass of a star as a reference unit for mass,  $M_0 = M_*$  and radius of the star as reference unit for length,  $R_0 = R_*$ .<sup>5</sup> Reference value for velocity is Keplerian velocity at radius  $R_0$ :  $v_0 = (GM_0/R_0)^{1/2}$ . The reference time scale is period of rotation at  $R_0$ :  $P_0 = 2\pi R_0/v_0$ . From dimensionalization of equations, we get ratio:  $\rho_0 v_0^2 = B_0^2$ , where  $B_0$  and  $\rho_0$  are the reference magnetic field and density at  $R_0$ . We take the reference magnetic field  $B_0$  such that the reference density is typical for considered types of stars (see Tab. 1). We then define the reference dipole moment  $\mu_0 = B_0 R_0^3$ , density  $\rho_0 = B_0^2/v_0^2$ , mass accretion rate  $\dot{M}_0 = \rho_0 v_0 R_0^2$ , energy per unit time  $\dot{E}_0 = \rho_0 v_0^3 R_0^2$ . Temperature  $T_0 = p_0/(\mathcal{R}\rho_0)$ , where  $\mathcal{R}$  is the gas constant.

We fix these reference units (and hence, the initial density, pressure, etc. distribution in the disc), but vary the initial magnetic field on the surface of the star and in the disc with dimensionless parameters  $B'_*$  and  $B'_d$  respectively<sup>6</sup>, so that the dimensional magnetic fields on the surface of the star (at the equator) is:  $B_* = B'_* B_0$  and initial field in the disc  $B_d = B'_d B_0$ .

The MHD equations are solved using dimensionless variables  $\tilde{r} = r/R_0$ ,  $\tilde{v} = v/v_0$ ,  $\tilde{t} = t/P_0$ ,  $\tilde{B} = B/B_0$ , and so on. In the subsequent sections, we show dimensionless values for all quantities and drop the tildes. Our dimensionless simulations are applicable to stars of different scales. We list the reference values for a few types of stars in Tab. 1. To derive the real, dimensional values, one needs to multiply the dimensionless values obtained from simulations by reference values presented in Tab. 1.

#### 2.4.3 Initial conditions

A rotating magnetized star of mass  $M_*$  and radius  $R_*$  is surrounded by an accretion disc and a corona. The disc is relatively cold and dense, while the corona is hot and rarefied. We set the temperature in the corona  $T_c = T_0$  and in the disc  $T_d = 0.01T_c$  (we determine these values at the inner edge of the disc, which is our reference point). The density in the disc and corona  $\rho_d = \rho_0$ ,  $\rho_c = 0.01\rho_d$ . Here, the subscripts 'd' and 'c' denote the disc and the corona. The initial density distribution is derived from the balance between the gravitational, centrifugal and pressure gradient forces, as well as

<sup>5</sup> The magnetospheric radius,  $r_m$  is another important scale of the problem, which is one of the main parameters used in theoretical investigations. However, in simulations it varies in time, and hence we use radius of the star as a reference unit, and obtain  $r_m$  from simulations.

<sup>6</sup> Note that parameter  $B'_*$  in this paper is identical to parameter  $\tilde{\mu}$  used in our previous papers (e.g., in Romanova et al. 2011a).

|  | CTTSs                 | White dwarfs         | Neutron stars        |
|--|-----------------------|----------------------|----------------------|
| $M_*(M_\odot)$                             | 0.8                   | 1                    | 1.4                  |
| $R_*$                                      | $2R_\odot$            | 5000 km              | 10 km                |
| $R_0$ (cm)                                 | $1.4 \times 10^{11}$  | $5.0 \times 10^8$    | $1.0 \times 10^6$    |
| $v_0$ (cm s <sup>-1</sup> )                | $2.8 \times 10^7$     | $5.2 \times 10^8$    | $1.4 \times 10^{10}$ |
| $T_0$ (K)                                  | $9.4 \times 10^6$     | $3.2 \times 10^9$    | $2.2 \times 10^{12}$ |
| $P_0$                                      | 0.37 days             | 6.1 s                | 0.46 ms              |
| $B_{*0}^{eq}$ (G)                          | $5 \times 10^2$       | $5.0 \times 10^5$    | $5 \times 10^8$      |
| $B_0$ (G)                                  | 50                    | $5.0 \times 10^4$    | $5.0 \times 10^7$    |
| $\rho_0$ (g cm <sup>-3</sup> )             | $3.3 \times 10^{-12}$ | $9.4 \times 10^{-9}$ | $1.3 \times 10^{-5}$ |
| $\dot{M}_0$ ( $M_\odot$ yr <sup>-1</sup> ) | $5.6 \times 10^{-8}$  | $1.9 \times 10^{-8}$ | $2.9 \times 10^{-9}$ |
| $\dot{E}_0$ (erg s <sup>-1</sup> )         | $1.3 \times 10^{33}$  | $3.2 \times 10^{35}$ | $3.4 \times 10^{37}$ |

**Table 1.** Sample reference values for typical CTTSs, white dwarfs, and neutron stars. The dimensional values can be obtained by multiplying the dimensionless values by these reference values.

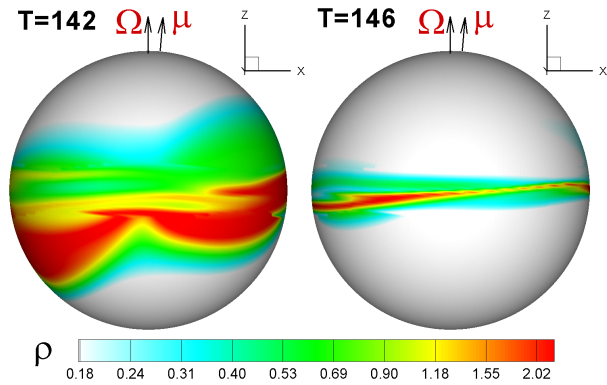


**Figure 5.** Density distribution in the hot spots at the surface of the star in the BL regime ( $B'_* = 0.001$ ) during the local maximum of the accretion rate,  $T = 142$  (left panel) and local minimum  $T = 146$  (right panel).

the condition that the corona rotates with the angular velocity of the disc and the gas is initially barotropic. In addition, the pressure is balanced at the boundary between the disc and corona. The resulting initial distributions of density in the disc and corona is almost homogeneous (within 10%). The density only slightly increases outward in both, disc, and corona. Distribution of the temperature (and the sound speed  $c_s$ ) is also almost homogeneous. In dimensionless units, initial values at the reference point are:  $\rho_d = 1$ ,  $\rho_c = 0.01$ ,  $T_d = 0.01$ ,  $T_c = 1$ .

The star rotates slowly with a fixed angular velocity  $\Omega_*$  such that the corotation radius  $r_{cor} = 10R_*$ , so that  $r_{cor}/r_m \approx$

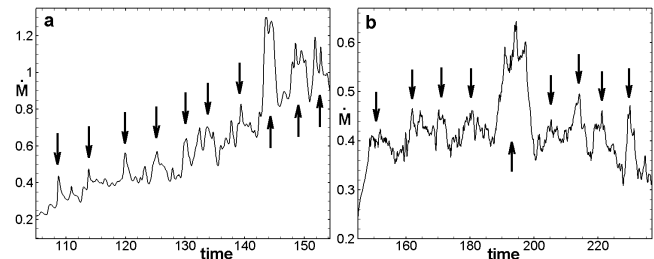


**Figure 6.** Accretion rate at the surface of the star in cases of the BL regime. Panels a and b show the cases of  $B'_* = 0.001$  and  $B'_* = 1$  respectively.

3. We take such a slow rotation to be sure that conditions are favorable for magnetospheric accretion during the whole simulation run, as we discussed in Sec. 2.2. Cases of more rapid rotation and the propeller regime will be investigated in the future.

A star has a dipole magnetic field. The strength at the equator is determined by the dimensionless parameter  $B'_*$ . The dipole moment is tilted at an angle  $\Theta$  about the rotational axis of the star (which is aligned with the rotational axis of the disc). Simulations show that at typical parameters of the disc, described above, the disc is truncated by the magnetosphere (and hence, the magnetosphere is dynamically important) if  $B'_* \gtrsim 1$ . At smaller values of the field, the magnetosphere is dynamically unimportant, and matter accretes in the BL regime. We take very weak field,  $B'_* = 0.001$ , for modelling the BL regime. We also take the marginal field,  $B'_* = 1$ , for test runs. A stronger field,  $B'_* = 10$ , is used for modelling the magnetospheric regime of accretion.

The disc and corona are threaded with a homogeneous small seed poloidal field. The strength of the field is determined by the dimensionless parameter  $B'_d$ . We take  $B'_d = 0.005$  in case of the BL regime, and  $B'_d = 0.01$  in case of the magnetospheric regime. Figure 2 shows the initial distribution of density and magnetic field in  $xz$ -slices in cases of the BL regime, where  $B'_* = 0.001$ ,  $\Theta = 5^\circ$  (left panel), and magnetospheric regime, where  $B'_* = 10$ , and the tilt is either large,  $\Theta = 30^\circ$  (middle panel), or very small,  $\Theta = 2^\circ$  (right panel).

Conversion of our dimensionless parameters to dimensional shows that the density, velocity, magnetic field and other parameters match well with those observed in typical stars listed in Tab. 1. However, the temperature in both, disc and corona, is about 10-20 times higher than that observed in real stars. In our initial setup, this is a consequence of the low density contrast between the disc and corona, which is initially  $\rho_c/\rho_d = 10^{-2}$ . At the higher density contrast,  $\rho_c/\rho_d = 10^{-3}$ , temperature is realistic, however these simulations require higher grid resolution and the simulation time is much longer. Realistic, much lower values for temperature in the disc and corona are used in *axisymmetric* simulations of  $\alpha$ -discs (e.g., Long et al. 2005) and MRI-driven discs (Romanova et al. 2011a). These simulations do not show any notable difference in results between high and low-temperature flows. We suggest that in both cases, the inner disc is sufficiently thick, so that the gravity force is the main force pulling matter to the funnel flow (if  $r_m < r_{\text{cor}}$ ). We discuss possible influence of the higher temperature in the disc to magnetospheric accretion in Sec. 4.1.

#### 2.4.4 Boundary conditions

At the outer boundary of the simulation region, we fixed all 8 variables. The boundary is located at  $R_{\text{out}} \approx 51R_*$  for the case of the BL regime and  $R_{\text{out}} \approx 32R_*$  for the magnetospheric regime. We observed from simulations that the disc is sufficiently large to supply matter during the whole simulation run.

At the inner boundary (which is a stellar surface) we take 'free' boundary conditions, which are corrected to the specifics of the considered problem. In general, the number of the boundary conditions should correspond to a number of waves propagating from the boundary to the simulation

region. However, the relationship between the radial velocity at the inner boundary and velocities of MHD waves is not known in advance. In addition, the interaction of the accreting matter with the stellar surface is a separate, complex problem, which requires detailed calculations of processes at much smaller scale<sup>7</sup>. Besides, matter can accrete, or, it can flow away from the star. We do not consider the complex processes near the stellar surface, but instead use simplified boundary conditions, which allow the absorption of matter which falls to the star's surface.

We consider two types of boundary conditions for different regimes of accretion. *Type A*: If the magnetic field of the star is dynamically unimportant and accretion is super-Alfvénic, then we use 'free' boundary condition for all variables:  $\partial U/\partial r = 0$  where  $U = s$  (entropy),  $\mathbf{v}$  (total velocity vector),  $\mathbf{B}_t$  (tangential to the stellar surface component of the field),  $r^2 B_r$  (normal to the surface component of the field multiplied by  $r^2$ ). We artificially decrease the pressure  $p$  at the inner boundary so that to stimulate accretion, and to remove excessive matter if it accumulates at the boundary:  $p_0 = kp_1$ ,  $k = 0.9$ , where the subscripts '0' and '1' mark the boundary grid and the last calculated cell respectively. The density in the boundary cell is recalculated as  $\rho_0 = (p_0/s_0)^{1/\gamma}$ . These conditions are used in the regime of the boundary layer accretion.

*Type B*: In case when the magnetic field is dynamically important, then the accreting flow is sub-Alfvénic (at the surface of the star) and two waves propagate from the boundary to the simulation region: Alfvén wave and fast magnetosonic wave. Hence, we provide two additional boundary conditions: in the coordinate system rotating with the star, the velocity vector is parallel to the magnetic field vector, which we split to two components: normal (or, radial) component,  $B_r$ , and the component tangential to the surface of the star,  $B_t$ . This condition means that the strong magnetic field acts as 'rails' attached to the non-deformed surface of the star along which matter flows to the star. We use the following algorithm to calculate these conditions: 1) we calculate the total vector of velocity in the boundary grid as  $\mathbf{v}'_0 = \mathbf{v}_1$ ; 2) we subtract rotation of the star:  $\mathbf{v}''_0 = \mathbf{v}'_0 - (\Omega_* \times \mathbf{r}_0)$ , where  $\mathbf{r}_0$  is the radius-vector of the center of the boundary grid, 3) we project vector  $\mathbf{v}''_0$  to the direction of the magnetic field:  $\mathbf{v}'''_0 = (\mathbf{B}_0 \mathbf{v}''_0)/B_0^2$ ; 4) we add to the velocity a part connected with rotation of the star:  $\mathbf{v}_0 = \mathbf{v}'''_0 + (\Omega_* \times \mathbf{r}_0)$ . We use these boundary conditions for modelling the magnetospheric regime.

#### 2.5 Number of MRI wavelengths per thickness of the disc

Before starting simulations, we estimate the expected number of MRI wavelengths within the thickness of the disc, using the analysis outlined in Sec. 2.3 and the dimensionless parameters of the model. The wavelength of the most unstable, MRI-driven mode is  $\lambda_{\text{MRI}} \approx 2\pi v_{A,z}/\Omega_K$ . In the approximation of the thin disc, the full thickness of the disc is  $2h \approx 2c_s/\Omega_K$ , where  $c_s = \sqrt{p/\rho}$  is the locally isothermal sound speed in the

<sup>7</sup> For example, interaction of the supersonic funnel stream with stellar surface leads to the formation of the radiative shock wave, which oscillates (e.g., Koldoba et al. 2008).

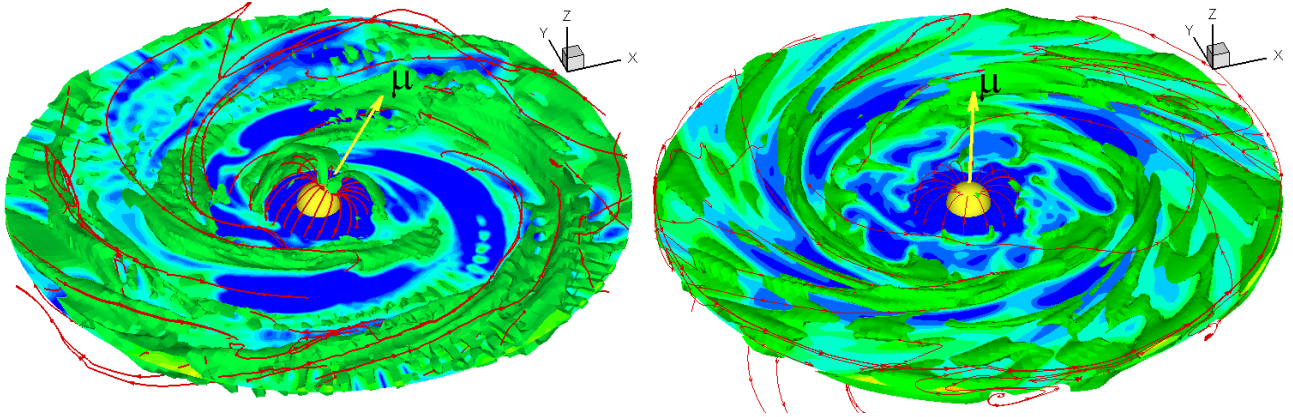


**Figure 7.** A three-dimensional view of accretion on to a star with a large magnetic field,  $B'_d = 10$ , at large  $\Theta = 30^\circ$  (left-hand panel) and small  $\Theta = 2^\circ$  tilts. The green background shows one of density levels, the blue color shows the equatorial density slice, and the lines are sample magnetic field lines.

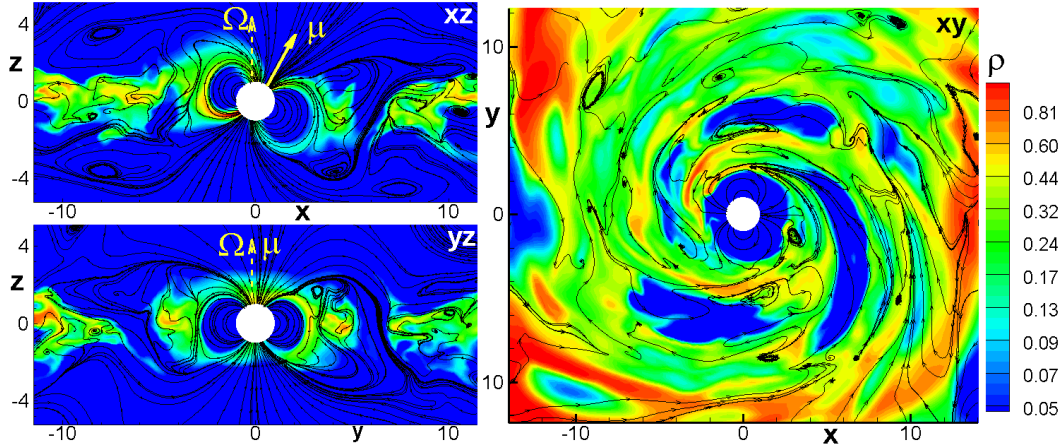


**Figure 8.** Slices of the density distribution (color background) and sample field lines in the case of a star with dynamically important magnetic field ( $B'_d = 10$ ) and large tilt ( $\Theta = 30^\circ$ ). The left-hand panels show the  $xz$  and  $yz$  slices, while the right-hand panel shows the equatorial slice,  $xy$ ,

disc. The number of wavelengths per thickness of the disc is  $N_{\text{MRI}} = 2h/\lambda_{\text{MRI}} \approx c_s/\pi v_{A,z}$ . In our model (in dimensionless units): density in the disc is  $\rho_d \approx 1$ , the sound speed is  $c_s \approx 0.1$ , the Alfvén velocity (based on  $B'_d = 0.01$  field) is  $v_{A,z} = B'_d/\sqrt{4\pi\rho_d} \approx 2.8 \times 10^{-3}(B'_d/0.01)(\rho_d/1.0)^{-1/2}$ . Substituting these values to the initial formula for  $N_{\text{MRI}}$  and to eq. 5, we obtain:

$$\beta = \frac{2c_s^2}{v_A^2} = 2.5 \times 10^3 \left(\frac{0.01}{B'_d}\right)^2 \left(\frac{\rho_d}{1.0}\right) \left(\frac{c_s}{0.1}\right)^2, \quad (5)$$

$$N_{\text{MRI}} = \frac{2h}{\lambda_{\text{MRI}}} = 11 \left(\frac{0.01}{B'_d}\right) \left(\frac{\rho_d}{1.0}\right)^{-1/2} \left(\frac{c_s}{0.1}\right). \quad (6)$$

These formulae are approximate but useful for understanding the start-up conditions for development of the instability. Below, we show results of our simulations in two different regimes: the BL regime, and regime of the magnetospheric accretion.

### 3 BOUNDARY LAYER REGIME

First, we investigate the case where the magnetic field of the star is dynamically unimportant and matter accretes to the star in the BL regime. We use this case to investigate the MRI-driven turbulence in the disc in our numerical setup. This case is also interesting from the astrophysical point of view, because many stars are expected to accrete in the BL regime. Below, we discuss both aspects of the problem.

#### 3.1 MRI-driven accretion

We investigated accretion at several values of the seed poloidal field in the disc from  $B'_d = 0.002$  up to  $B'_d = 0.01$ , and found that in all cases the MRI-driven turbulence is developed, matter accretes inward, and angular momentum is transported outward by the magnetic shear stress (see details is Sec. 5). In experiments with the smallest in the set magnetic field,  $B'_d = 0.002$ <sup>8</sup>, the initial number of wavelengths

<sup>8</sup> We used this field as a base in axisymmetric simulations (Romanova et al. 2011a).

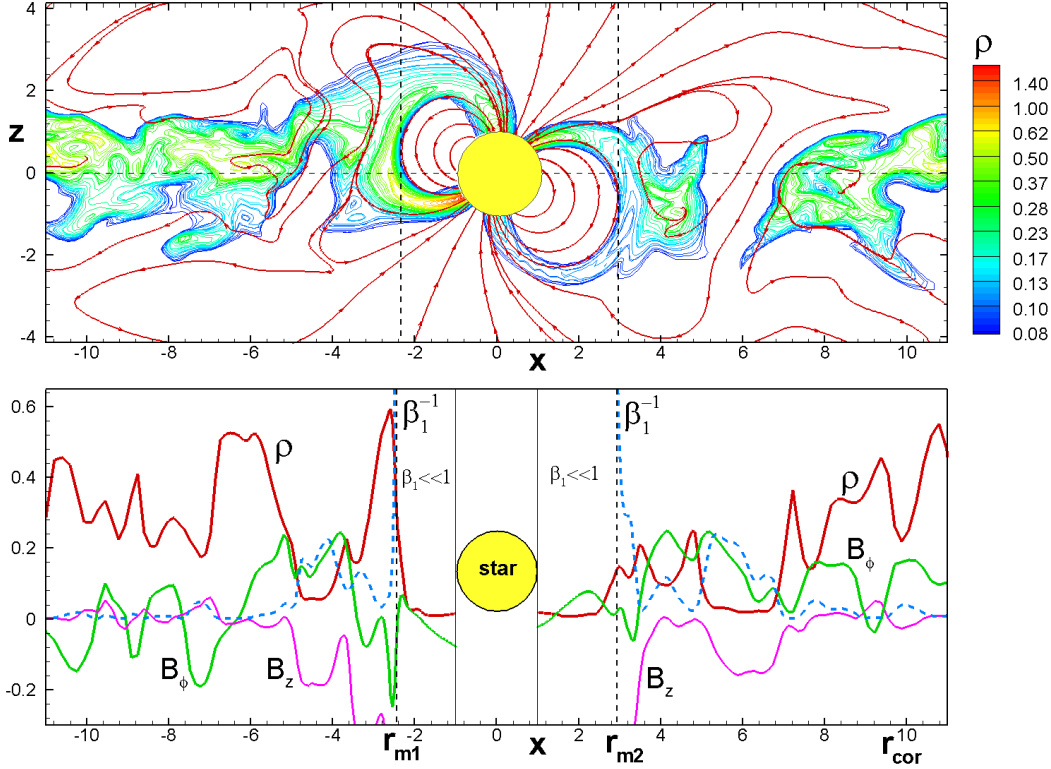


**Figure 9.** *Top panel:* The density distribution in the inner disc and in funnel streams in the  $xz$ -plane and selected field lines. *Bottom panel:* Linear distributions of different variables in  $x$ -direction in the equatorial plane: the density,  $\rho$ , two components of magnetic field,  $B_z$  and  $B_\phi$ , and  $\beta_1^{-1}$ . The dashed vertical lines correspond to  $\beta_1 = 1$  and show the position of the magnetospheric radius to the left,  $r_{m1}$  and to the right,  $r_{m2}$ , of the star. The position of the corotation radius,  $r_{cor}$ , is also shown.

per thickness of the disc is relatively large,  $N_{MRI} = 55$  (at the inner disc), but the accretion rate, which is proportional to the magnetic stress in the disc, is low: matter of the inner disc reaches the star in  $T \approx 200$  rotations (at  $r = 1$ ). These simulations last up to  $T \approx 800$ . In the case of the largest field,  $B'_d = 0.01$  ( $N_{MRI} = 11$ ), the accretion rate is high, however only 1-2 turbulent cells per thickness of the disc are observed in developed turbulence.<sup>9</sup> We take the intermediate field,  $B'_d = 0.005$ , as a base for simulations, because the accretion rate is relatively high, and at the same time, a few turbulent cells per thickness of the disc are observed.

We also varied the magnetic field of the star from very weak,  $B'_* = 0.001$  (and dynamically insignificant during the whole simulation run), to somewhat stronger,  $B'_* = 1$ , where a tiny magnetosphere was observed initially, but it disappeared later, when the accretion rate became larger.

The initial density and temperature distribution in the disc is almost homogeneous (within 10%), and the magnetic field threading the disc and corona is a constant (see Fig. 2, left panel, and Sec. 2.4.3). As a result, the initial distribution of  $\beta$ -parameter in the disc is almost homogeneous, and for the disc field of  $B'_d = 0.005$ , it is  $\beta \approx 9,000$ . We observed, that the initial number of wavelengths per thickness of the disc is  $N_{MRI} \approx 10 - 20$ , as predicted by the theory

(see Sec. 2.5). Subsequently, the perturbations grow due to the magneto-rotational instability, and turbulence develops in the inner parts of the disc (at  $T \approx 10 - 20$  periods of rotation at  $r = 1$ ). Later, turbulence develops at larger radii. Subsequently, the magnetic energy in the disc increases, mainly due to the growth of the azimuthal component of the field, which leads to strong decrease of  $\beta$ . As a result, the number of turbulent cells per thickness of the disc decreases up to 2-3.

Figure 3 shows slices of the density distribution at  $T = 150$ . The left-hand panels show that the flow is turbulent, and the poloidal field lines are tangled and have a number of reversals which track different turbulent cells. The right-hand panel of Fig. 3 shows the equatorial slice of the density distribution. One can see that the turbulent cells are strongly elongated in the azimuthal direction, and they also look like parts of spiral waves.

### 3.2 Azimuthally-wrapped magnetic field in the inner disc

In the inner parts of the disc, the azimuthal magnetic field increases rapidly due to strong shear in the flow. In addition, the poloidal magnetic field increases towards the inner disc due to the convergence of the flow and conservation of the poloidal magnetic flux. As a result, the azimuthal component of the field reaches the value of  $B_\phi \approx 1$  which is about 200 times larger than the initial seed poloidal field of  $B'_d = 0.005$ . The plasma parameter  $\beta$  drops to  $\beta \approx 1 - 3$ , that is, the magnetic and thermal pressure are close to the equipartition state.

<sup>9</sup> Note, that the initial value of  $N_{MRI}$  is based on the *initial* seed poloidal field in the disc. Subsequently, the azimuthal component increases, and the number of turbulent cells per thickness of the disc drops.



Fig. 4 (right panel) shows the distribution of the magnetic pressure scaled to matter pressure,  $\beta^{-1} = B^2/8\pi p$  at  $t = 150$ . The thick black line shows exact equipartition, where  $\beta = 1$ . One can see elongated islands, where the magnetic pressure dominates (yellow and red color). The left-hand panel shows the  $xz$ -slice, where the turbulent cells are seen in their cross-sections. These simulations are in accord with earlier simulations by Armitage (2002) and by Steinacker & Papaloizou (2002), who also observed strong amplification of the field in the inner disc.

Pringle (1989) argued that magnetic flux built up in the disc should escape to the corona due to the Parker instability, and that this field can be responsible for magnetically-driven outflows from young stars (see also Shu et al. 1988). Formation of the magnetically-dominated corona has been observed in 3D simulations (e.g., Miller & Stone 2000; Hawley et al. 2002). Very long-lasting axisymmetric simulations by Romanova et al. (2011a) performed at 10 times lower density in the corona (compared with present simulations) show the formation of a very large magnetic corona which slowly moves away from the disc to large distances, and which is driven by the magnetic force (see fig. 20 and 21 of Romanova et al. 2011a). In the present simulations, we have not seen such a corona, because the matter density in the corona is too high, and simulations are not as long. We expect that the large-scale expanding magnetic corona will be seen in the future 3D simulations. Formation of faster outflows from the disc-star boundary, as discussed by Pringle (1989), also can not be excluded.

We also observed an interesting phenomenon, that the magnetic flux of the star increases in time, and a new magnetosphere forms around the star. The initially weak magnetic field of  $B'_* = 0.001$  increased up to  $B_* \approx 1$  (at the pole, above the star) because the accreting matter brings the poloidal field towards the star, and this field is accumulated at the stellar surface. Fig. 4 (left panel) shows that the new magnetosphere has a monopole-type shape. The magnetosphere does not truncate the disc<sup>10</sup>, and the disc accretes in the BL regime. We suggest that in longer simulation runs, the magnetic field can increase up to even larger values. On the other hand, the disc can bring matter with the field of one or another polarity, and the induced magnetic field of the star will flip its polarity.

Of, course, details of the disc-star interaction depend on the boundary conditions at the star. Here, we show results for one type of boundary conditions (*Type A*, see Sec. 2.4.4), where both, matter and magnetic field can accrete on to the surface of the star. However, conditions at the boundary can be different. For example, if a star is a perfect conductor, then the magnetic flux of the disc will not penetrate through the star, but instead it will accumulate at the disc-star boundary. Such a condition will be more favorable for formation of the magnetic torus, and/or for outflows.

<sup>10</sup> Note that the field  $B'_* \approx 1$  corresponds to the border between dynamically active and passive magnetospheres.

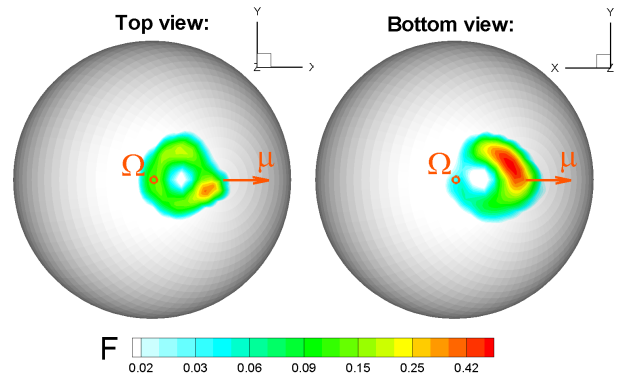


**Figure 10.** Distribution of the kinetic energy flux in the hot spots at the surface of the star as seen from the top ( $-z$ -direction, left-hand panel) and the bottom ( $+z$ -direction, right-hand panel).

### 3.3 Equatorial belt spots and variability associated with accretion of turbulent cells

In the BL regime, the disc matter accretes to the star in the region of the equator, and it forms the belt-shaped hot spot. About a half of the gravitational energy of the accreting matter is expected to be released in the equatorial belt spot. The details of the physics of the disc-star interaction including the processes of the heating and cooling of matter in the BL are not established. The interaction may include complex processes such as the Kelvin-Helmholtz instability and the formation of a turbulent layer at the surface of the star. One can expect, however, that most of energy will be released in regions of enhanced density. This is why we show the density distribution at the star's surface.

We observed in simulations that matter accretes onto the star in azimuthally-stretched turbulent cells. Near the star, the turbulent cell becomes stretched in the azimuthal direction, and when it accretes on to the star, it forms the higher-density spot which is also spread in the meridional direction. The spots are less dense and more narrow during periods of lower accretion rate.

Fig. 5 (left panel) shows the density spot during accretion of one of the turbulent cells. The spot is not symmetric, because the turbulent cell is not azimuthally-symmetric. The spot is quite wide in the meridional direction. The right panel shows the spot during period of the minimum of the accretion rate, when one of cells already accreted, while another one did not approach the star yet. This spot is more narrow in the meridional direction.

Accretion of turbulent cells leads to *variability* of the accretion rate at the star. Fig. 6 shows the accretion rate for our reference case with initial stellar field of  $B'_* = 0.001$  (left panel), and in the case of larger initial field of the star,  $B'_* = 1$  (right panel). For these cases, we used boundary conditions of *Type A* and *Type B* respectively (see Sec. 2.4.4). We observed that the peaks in the accretion rate (see arrows in the plot) correspond to the accretion of individual turbulent cells. The accretion rate is typically about 20% higher than the average during accretion of a turbulent cell, and the maxima at 50% correspond to the accretion of the largest turbulent cells. The time interval between peaks in these two cases is  $\Delta t \approx 5$  and  $\Delta t \approx 10$ , respectively. The accretion rate curves are quite similar in spite of the different initial fields of the star and some-

what different boundary conditions. Note that we have the same initial conditions in discs, and hence the MRI-induced turbulence in the disc has the same properties. This may determine the similarity in the time-scale between peaks. Some difference is connected with different conditions at the star.

In our simulations, we observe quite large turbulent cells, and hence we observe and ‘count’ them during their accretion on to the star. Such turbulence dominates in discs which are close to equipartition with  $\beta \sim 1$ . We suggest, that equipartition is a probable state in the inner regions of accretion discs where the shear is high. In the opposite case,  $\beta \gg 1$ , multiple turbulent cells are present in the disc. The simultaneous accretion of multiple cells will lead to much smoother accretion, and results will be closer to those observed in cases of  $\alpha$ -discs (e.g., Romanova et al. 2004). Hence, the variability pattern carries information about the property of the turbulence in the disc.

#### 4 REGIME OF MAGNETOSPHERIC ACCRETION

Next, we discuss accretion on to stars with *dynamically important* magnetic fields, where the disc is truncated by the magnetosphere of the star and matter accretes in funnel streams. We chose the parameter  $B'_* = 10$  for these runs. We investigate cases of large ( $\Theta = 30^\circ$ ) and small ( $\Theta = 2^\circ$ ) tilts of the dipole magnetic moment relative to the rotational axis. To save computing time, we increased the seed magnetic field in the disc up to  $B'_d = 0.01$ . This helped to increase the accretion rate (which is proportional to the magnetic stress in the disc), and cause the disc to reach the surface of the star more rapidly, at about  $T = 40^{11}$ .

We observed that initially, about 10 MRI wavelengths fit within the vertical extent of the disc, and the inner parts of the disc started accreting towards the star. Later, the azimuthal field increased, and the number of turbulent cells observed later in simulations dropped to 1-2 per thickness of the disc.

Figure 7 shows a 3D view of the MRI-driven discs in cases of low and high tilts of the dipole field. The background shows one of density levels. One can see that in both cases, the disc is strongly inhomogeneous: matter tends to be concentrated in azimuthally-elongated spiral segments. The magnetic field lines are stretched in the azimuthal direction. Below, we consider these two cases in greater detail.

##### 4.1 Accretion on to a star with a large tilt, $\Theta = 30^\circ$

In the case of a large tilt of the dipole field, matter flows to the star in funnel streams. Figure 7 (left panel) shows such an accretion flow, where matter of the disc accretes to the star in funnel streams. These funnel streams form when a large turbulent cell moves towards the magnetosphere, where it is stretched, slowed down by the magnetosphere, and pulled towards the star by the gravity force.

Figure 8 (left two panels) shows  $x - z$  and  $y - z$  slices of density distribution and the poloidal magnetic field. One can see that the disc is truncated and matter flows to the star in funnel streams. The height of the magnetosphere is only

slightly larger than the height of the turbulent disc. The regions of enhanced density in the disc (yellow and red colors) track the turbulent cells. We observed accretion of several turbulent cells during the simulations.

The field lines threading the disc inflate into the corona. The accretion disc compresses the external field lines and pushes them to reconnect. After reconnection, the magnetic islands form and propagate into the corona. This process of compression and reconnection is similar to that observed in axisymmetric simulations (Romanova et al. 2011a). Reconnection acts as an efficient means of diffusivity, and it helps the disc to penetrate through the external layers of the magnetosphere of the star towards the closed magnetosphere and to the star through the funnel flow.

The right-hand panel of Fig. 8 shows that the magnetic field has a significant azimuthal component, and the turbulent cells are elongated in the azimuthal direction. The tilted rotating dipole excites two spiral waves in the inner disc. These waves are similar to those observed in 3D simulations of  $\alpha$ -discs with a tilted dipole magnetic field (Romanova et al. 2011b).

Figure 9 (top panel) shows the disc-magnetosphere boundary in greater detail. One can see that the disc is turbulent. It is disrupted by the stellar magnetosphere and the matter flows towards the star forming a funnel flow. One can see that the funnel streams are not symmetric: the accretion rate is higher from the left side than from the right side. This is in contrast with earlier 3D simulations of accretion from  $\alpha$ -discs, where the funnel streams are symmetric (see, e.g., Fig. 4 from Romanova et al. 2004). The asymmetry is connected with the fact that matter approaches the magnetosphere of the star and then accretes in large-scale turbulent cells, which are usually closer to one of poles than to another. Fig. 7 (left panel) shows a typical process of accretion of the turbulent cell.

The bottom panel of Fig. 9 shows the distribution of different variables in the equatorial plane. One can see that the density  $\rho$  is highly variable in the inner disc, and it is very small inside the magnetically-dominated magnetosphere. The azimuthal component of the field,  $B_\phi$ , is a few times larger than  $B_z$ -component. Inside the magnetosphere, the toroidal field is much smaller than the poloidal field.

The inner radius of the disc coincides with the point where our modified plasma parameter  $\beta_1$  (eq. 2) is unity. The vertical dashed lines in Fig. 8 show the radii where  $\beta_1 = 1$ . One can see that the magnetospheric radius to the left of the star,  $r_{m1} \approx 2.4$  is smaller than to the right,  $r_{m2} \approx 3$ . The asymmetric nature of the magnetospheric surface is also seen in Fig. 8 (right panel). Top panel of the Figure also shows that the funnel streams have a finite width and some matter start flowing to the funnel from larger radii,  $r \approx 3 - 4$ .

Matter moves to the funnel flow due to the gravitational force, which dominates over the centrifugal force (in our case of a slowly rotating star). The lifting of matter to  $|z| > 0$  to the funnel starts at the radius where the azimuthal motion of the inner disc matter slows down due to interaction with the magnetosphere. This occurs at  $r \approx 4 - 5$ . The magnetosphere is small, while the disc is has a finite thickness due to the turbulent nature of the flow. Hence the magnetosphere is

<sup>11</sup> Simulations with a field of  $B'_d = 0.005$  produce similar results, but on a longer time scale.

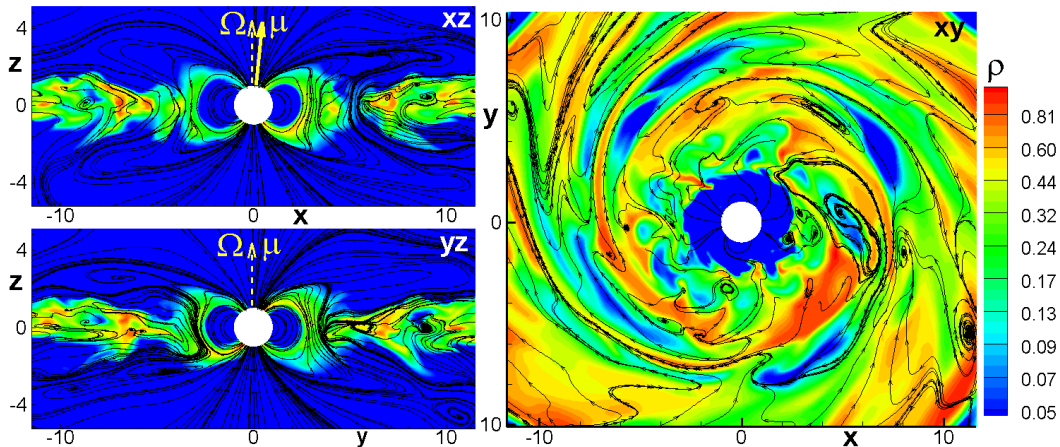


**Figure 11.** Slices of the density distribution (color background) and sample field lines in the case of a star with dynamically important magnetic field ( $B'_d = 10$ ) and high tilt ( $\Theta = 2^\circ$ ). The left-hand panels show the  $xz$  and  $yz$  slices, while the right-hand panel shows an equatorial, slice,  $xy$ .

not a big obstacle for the flow of matter towards the star<sup>12</sup>. The matter pressure gradient force also contributes to the lifting, though the role of this force is not as significant as in the case of the *aligned* dipole (e.g., Romanova et al. 2002 and Campbell 2010). Note, that axisymmetric simulations of MRI-driven accretion were performed at much lower, realistic temperature in the disc and corona, and did not show principal difference between higher and lower temperature cases (Romanova et al. 2011a). Moreover, in case of a tilted dipole, the magnetic field lines are inclined in the equatorial plane, and hence the star's gravitational force can pull matter directly from the equatorial plane of the disc.

Note, that inside the disc, the total matter stress is much larger than the magnetic stress,  $\beta_1 \gg 1$ , and the disc acts as matter-dominated (see also Sec. 5). The MRI-driven instability, initiated by the initial seed field in the disc, provides inward transport of matter, which can be roughly described as an effective ‘viscosity’. However, it does not provide diffusivity at the disc-magnetosphere boundary. The magnetic field of the star does not thread the incoming disc and does not influence to the MRI processes inside the disc. As a result the matter-dominated disc compresses the magnetosphere and pushes it to reconnect as shown in Fig. 8 and Fig. 9. It also penetrates toward the closed magnetosphere due to instabilities.

The funnel stream hits the surface of the star with a high velocity and the kinetic energy of the flow is released. Figure 10 shows the distribution of the kinetic energy flux in the hot spots on the surface of the star due to the impact of the funnel streams. One can see that the spots forming at the south and north hemispheres of the star are different. The difference between spots reflects the difference between funnel streams approaching the south and north hemispheres. Note, that hot spots obtained in 3D simulations of  $\alpha$ -discs, are almost identical (Romanova et al. 2004). Inequality of spots in the case of turbulent discs may have important consequences for analysis of variability from accreting magnetized stars.

#### 4.2 Accretion on to a star with small tilt, $\Theta = 2^\circ$ and interchange instability

Here, we discuss results for the case of very small tilt,  $\Theta = 2^\circ$ . Figure 11 (left panels) shows that the magnetosphere inflates in an almost symmetrical fashion. The magnetic flux inflates sideways, as we observed in axisymmetric simulations (Romanova et al. 2011a). This is because the time scale of disc accretion is smaller than the inflation time scale. The magnetic field in the inflated and stretched corona reconnects, while magnetic islands form and propagate outward.

The right-hand panel of Fig. 11 shows an equatorial slice. One can see that the magnetosphere with such a small tilt does not excite strong spiral waves. However, we observed another interesting phenomenon: matter of the disc located at large distances from the star penetrates through the magnetic field of the star in thin dense filaments. This is a sign of interchange (or magnetic Rayleigh-Taylor) instability. Fig. 7 (right panel) also shows these filaments. The filaments are tall (in the vertical direction) and narrow (in the radial direction). This shape is favorable for penetration between the field lines. This situation is analogous to penetration of disc matter through a vertical magnetic field threading the disc. This was investigated earlier with analytic theory and MHD simulations (Kaisig et al. 1992; Spruit et al. 1995; Lubow & Spruit 1995). Here, we observe this phenomenon in simulations<sup>13</sup>. The interchange instability can be an important mechanism of matter penetration through the magnetic field in accretion discs in different situations. It can give an enhanced transport of magnetic flux.

Matter of the disc which reaches the disc-magnetosphere boundary, can further penetrate through the *magnetically-dominated* magnetosphere due to same instability (e.g., Arons & Lea 1980; Spruit & Taam 1990; Li & Narayan 2004) or due to the Kelvin-Helmholtz instability (e.g., Lovelace et al. 2010). Our earlier global simulations of  $\alpha$ -type discs have

<sup>12</sup> Note, that the situation is different in cases of much large magnetospheres of X-ray pulsars and strongly magnetized white dwarfs in cataclysmic variables, where the height of the magnetosphere may be orders of magnitude larger than the thickness of the disc.

<sup>13</sup> Such an instability has been also observed in global 3D MHD simulations by Igumenshchev (2008), where the magnetic flux was accumulated in the inner parts of the disc around the black hole (see also Narayan et al. 2003).

shown that in magnetized stars matter flows towards the stellar surface either through two ordered funnel streams, above the magnetosphere, where two hot spots form, and the light curve is almost sinusoidal. Or, it can penetrate the magnetosphere due to interchange instability in the equatorial plane in narrow and tall ‘tongues’. In this case, a number of temporary hot spots form in random places, and the light-curve is chaotic (Romanova et al. 2008; Kulkarni & Romanova 2008). This has an important application for understanding of periodic and quasi-periodic variability in different stars with small magnetospheres (e.g., Kulkarni & Romanova 2009; Bachetti et al. 2010).

There are several factors which determine the boundary between the stable and unstable regimes of accretion. The unstable regime is favorable, if the magnetic axis has a small tilt about the rotational axis, if a star rotates slowly (hence, the gravitational plus centrifugal potential is negative), and also if sufficient amount of matter is accumulated at the disc-magnetosphere boundary. More, precisely, the theoretical condition for instability which agrees well with results of simulations requires that the gradient of the surface density  $\Sigma$  per unit of the vertical magnetic field  $B_z$  should be large and positive,  $d(\Sigma/B_z)/dr > 0$  (e.g., Spruit et al. 1995; Kulkarni & Romanova 2008). This term is required to overcome the stabilizing effect of the velocity shear (see, e.g., eq. 59 of Spruit et al. 1995).

In the present simulations, we see that matter is lifted above the magnetosphere and accretes in funnel streams (see Fig. 11, left panels). However, this is the case, which is favorable for the accretion though instabilities: the star rotates slowly, and the tilt  $\Theta = 2^\circ$  is very small. It is possible however that a high disc temperature (see Sec. 2.4.3) drives matter to the funnel flow and hence opposes to the onset of the instability. However, this is not the case, because in the  $\alpha$ -disc models (e.g., Romanova et al. 2008), where instability is observed, we used the *same parameters* for the density and temperature distribution in the disc and corona. We suggest the instability is not seen in the current simulations, because the runs are not long enough. There is not enough time to build up the radial gradient of  $(\Sigma/B_z)$  needed to trigger the instability. Note also that conditions for the onset of the interchange instability may be different in case of a turbulent disc.

## 5 ANALYSIS OF STRESSES IN THE DISC

In both cases considered above the turbulent accretion is excited by the magneto-rotational instability. Here, we analyze stresses in the disc. We separate the disc from the low-density corona using a specific density level,  $\rho_{disc} = 0.3$ , which is typical for the boundary between the disc and corona. We integrate the matter (subscript ‘m’) and magnetic (subscript ‘f’) stresses across the disc (in the  $z$ -direction) and obtain

$$\langle T_m \rangle = \frac{1}{2h} \int dz \rho v_r v_\phi - \langle \rho v_r \rangle \langle v_\phi \rangle,$$

$$\langle T_f \rangle = -\frac{1}{2h} \int dz \frac{B_r B_\phi}{4\pi}.$$

Here

$$\langle v_\phi \rangle = \frac{1}{2h} \int dz v_\phi, \quad \langle \rho v_r \rangle = \frac{1}{2h} \int dz \rho v_r$$

are averaged azimuthal velocity and matter flux, and  $h = h(r)$  is the half-thickness of the disc. Note that  $r\langle T_m + T_f \rangle$  is the radial angular momentum flux in the disc.

The matter and magnetic pressures are

$$\langle P_m \rangle = \frac{1}{2h} \int dz P, \quad \langle P_f \rangle = \frac{1}{2h} \int dz \frac{\mathbf{B}^2}{8\pi}.$$

The standard  $\alpha$ -parameters associated with matter and magnetic stresses are:

$$\alpha_m = \frac{2\langle T_m \rangle}{3\langle P_m \rangle}, \quad \alpha_f = \frac{2\langle T_f \rangle}{3\langle P_f \rangle}.$$

Figure 12 (left-hand four panels) shows the equatorial distribution of different averaged values in the disc for the case of the boundary layer accretion, where the magnetic field is relatively weak ( $B'_* = 0.001$ ). One can see that the magnetic stress,  $\langle T_f \rangle$ , is larger than matter stress,  $\langle T_m \rangle$ , and hence angular momentum is transported by the magnetic stress. Note that the matter stress also results from magnetic turbulence. It is interesting that the magnetic stress forms a clear one-armed spiral wave. The same wave is seen as a low-density pattern in Fig. 3. Slices for  $\alpha$ -parameters ( $\alpha_f$  and  $\alpha_m$ ) repeat the pattern for stresses. The four right-hand panels of Fig. 12 show the distribution of stresses along the  $x$  and  $y$  axes in the equatorial plane. One can see that the magnetic stress is larger on average than the matter stress in both the  $x$  and  $y$  directions. Its distribution is very inhomogeneous and it reflects the distribution of matter and magnetic stresses. The  $\alpha$ -parameters are also strongly inhomogeneous, and they track the regions of enhanced stresses. The maximum values are high:  $\alpha_f \approx 0.2 - 0.35$  and  $\alpha_m \approx 0.05 - 0.18$ .

Figure 13 (left-hand four panels) shows the equatorial distribution of different averaged values in the disc in the case of the magnetospheric accretion where the magnetic field is relatively strong and the tilt of the magnetic moment is high:  $B'_* = 10$ ,  $\Theta = 30^\circ$ . Here, we see that the equatorial distribution of stresses and  $\alpha$ -parameters has a similar pattern. The magnetic stress does not repeat the clear two-armed pattern observed in the density distribution (see Fig. 8).

The matter pressure is much higher than the magnetic pressure (because the temperature in the disc is relatively high due to the initial conditions). However, the magnetic stress is larger than matter stress at most of radii.

The bottom left-hand panels show that the magnetic and matter  $\alpha$ -parameters ( $\alpha_f$  and  $\alpha_m$ , respectively) repeat the pattern of the magnetic and matter stresses. The bottom right-hand panels show that the  $\alpha_f$  parameter is largest in spiral waves, ( $\alpha_f \approx 0.1 - 0.3$ ), and it is much smaller between them and at larger distances. The matter  $\alpha$ -parameter,  $\alpha_m$ , is much smaller than  $\alpha_f$ .

Note that the simulations in the case of a weak stellar magnetic field,  $B'_* = 0.001$ , run longer than in the case of a strong field. This may explain the formation of clear spiral features in spite of the small tilt of the magnetic moment,  $\Theta = 5^\circ$ . In the future, longer simulations runs may show further growth of the magnetic energy in the disc and more developed spiral structure.

## 6 CONCLUSIONS AND DISCUSSION

We performed global three-dimensional ideal MHD simulations of MRI-driven accretion on to magnetized stars with the

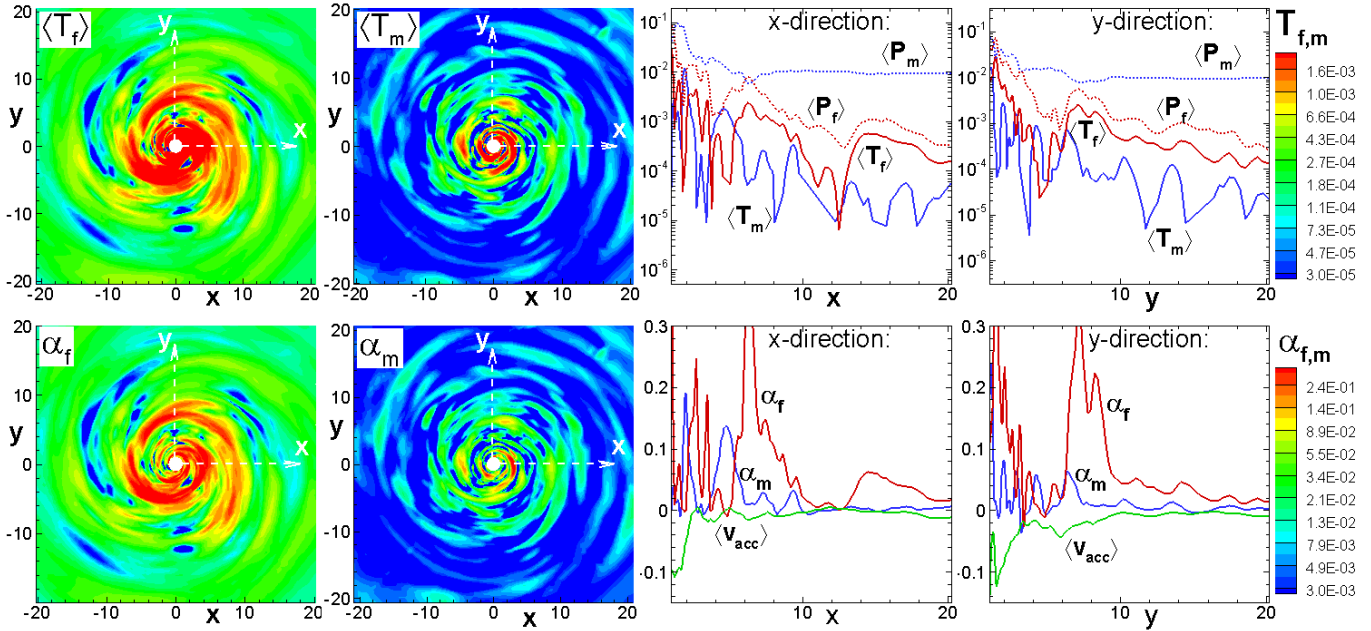


**Figure 12.** The integrated stresses, pressure and  $\alpha$ -parameters associated with matter ( $\langle T_m \rangle$ ,  $\langle P_m \rangle$ ,  $\alpha_m$ ) and the magnetic field ( $\langle T_f \rangle$ ,  $\langle P_f \rangle$ ,  $\alpha_f$ ) in the model with  $B_* = 0.001$  and  $\Theta = 5^\circ$ . *Left two panels:* the equatorial distribution. *Right two panels:* distribution along the  $x$  and  $y$  axes.

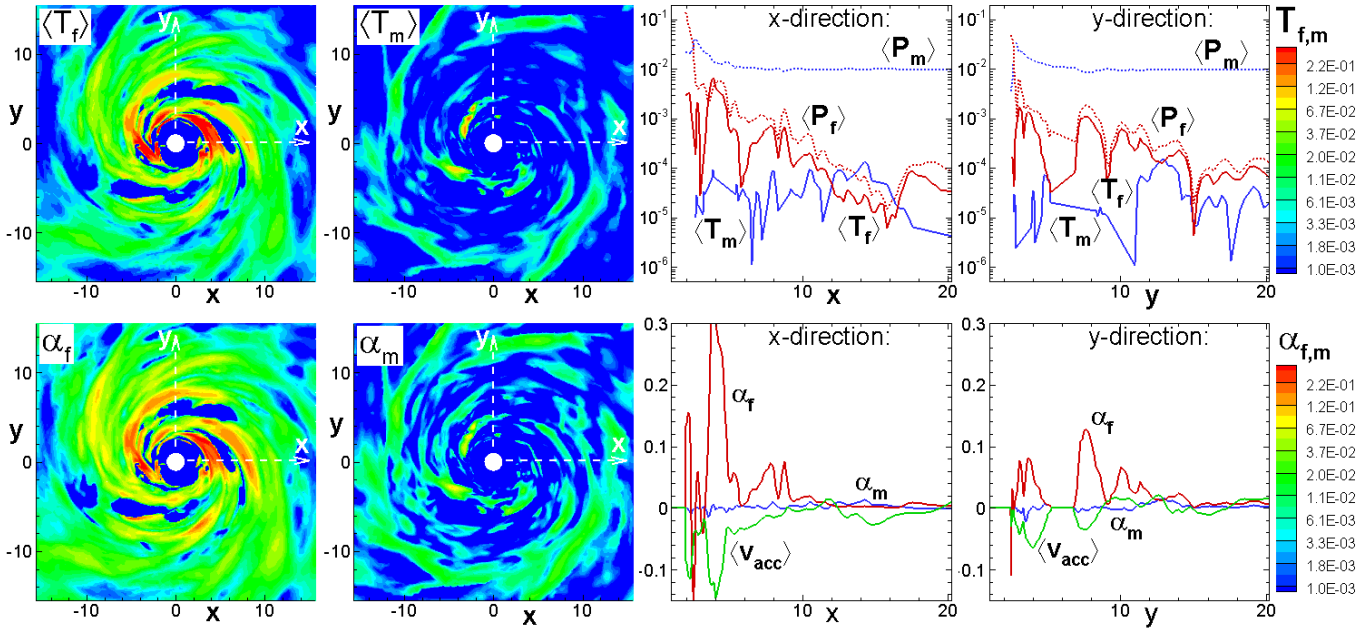


**Figure 13.** Same as in Fig. 12 but for the case with  $B_* = 10$ ,  $\Theta = 30^\circ$ .

dipole magnetic fields tilted at an angle  $\Theta$  relative to the stellar rotational axis (which coincides with the rotational axis of the disc). We use the version of our cubed sphere code (Koldoba et al. 2002) where the grid is compressed near the equatorial plane. Simulations were performed in dimensionless form and can be applied to different types of stars with relatively small magnetospheres, such as CTTs, accreting brown dwarfs, millisecond pulsars, and dwarf novae.

Multiple simulation runs were performed for different parameters of the star and the disc. However, for clarity we

show results for two main regimes of accretion. In one of them, the magnetic field of the star is dynamically unimportant: it does not stop the disc, and matter accretes to the surface of the star in the BL regime. In another regime, the magnetic field is dynamically important, it truncates the disc, and magnetospheric accretion is observed.

Common features observed in both regimes of accretion are the following:

(i) We observed that the MRI-driven turbulence develops in the disc and it is similar to that observed in cases of acce-

tion on to non-magnetized objects (black holes) (e.g., Hawley et al. 2001). The magnetic stress in the disc is larger than the turbulent part of matter stress, and hence, the angular momentum is transported outward by the magnetic stress.

(ii) The disc is strongly inhomogeneous: it consists of multiple azimuthally-elongated turbulent cells. The azimuthal field is about 10 times larger than the poloidal field.

(iii) The spiral structure is observed in the density and stress distributions in the disc. It is more prominent in the case of strongly tilted, dynamically important field ( $B'_* = 10$ ,  $\Theta = 30^\circ$ ), and in case of the dynamically unimportant field ( $B'_* = 0.001$ ,  $\Theta = 5^\circ$ ) where simulations are longer.

Below, we show main results for our two regimes of accretion:

*Boundary Layer regime:*

(iv) The magnetic field of the *inner disc* is strongly amplified due to the shear. The magnetic pressure becomes comparable with matter pressure,  $\beta \approx 1 - 3$ , and hence the inner disc is almost in the equipartition. This result is in accord with earlier simulations by Armitage (2002) and Steinacker & Papaloizou (2002), who also observed strong amplification of the field in the inner disc.

(v) Matter of the disc accretes to the star in individual turbulent cells. Accretion of the turbulent cell leads to formation of the density ‘spot’ on the star which has a shape of the equatorial belt. The belt is inhomogeneous and it is wide in the meridional direction. Spots have lower density and are more narrow during periods of lower accretion rate.

(vi) The matter flux at the surface of the star varies, and the maxima in the variability curve correspond to accretion of individual turbulent cells. The process is quasi-periodic with a period of a few Keplerian rotation periods at the radius of the star.

(vii) The accreting matter brings the poloidal magnetic flux to the star, and a weakly magnetized star acquires a new, ‘induced’ magnetosphere. The polarity of the induced field depends on the polarity of the disc field, and hence the field of the star can flip its polarity.

*In the Magnetospheric regime:*

(viii) The disc is truncated by the magnetosphere of the star at a few stellar radii, where the magnetic stress in the magnetosphere balances the total matter stress in the disc. Closer to the star matter flows to the star’s surface through the funnel streams.

(ix) The funnel streams flowing towards the south and north hemispheres are different, because the accreting turbulent cell flows mainly to the closest magnetic pole, and less matter flows to another pole.<sup>14</sup>

(x) The hot spots on the star are also different. They reflect the energy distribution in funnel streams.

(xi) In the case of a small tilt,  $\Theta = 2^\circ$ , matter of the disc penetrates through the external magnetosphere of the star due to the interchange instability. We suggest that this instability can also play an important role in further penetration of the disc matter through the closed, magnetically-dominated

magnetosphere. Further work is required to investigate this process.

One of important feature of accretion from turbulent discs (compared with  $\alpha$ -discs) is that the turbulence breaks the symmetry between two funnel streams and hot spots in case of magnetospheric accretion, and it brings non-axisymmetry to the shape of the equatorial belt in case of the boundary layer accretion. This property is important for understanding the light-curves from magnetized and non-magnetized stars.

The further enhancement of the magnetic field at the disc-star boundary, may possibly lead to the formation of a magnetic equatorial torus (Paczynski 1978) which has been used in the phenomenological models of quasi-periodic oscillation in dwarf novae cataclysmic variables (Warner 2003; Pretorius 2006). On the other hand, the build up of magnetic field may flow in to the corona due to the magnetic pressure force (see, e.g., Miller & Stone 2000; Romanova et al. 2011a) and it may be responsible for outflows from young stars (Pringle 1989, see also Shu et al. 1988). Recent axisymmetric simulations show formation of powerful, magnetically-driven outflows from the disc-magnetosphere boundary, where the strong magnetic field of the star is compressed by the disc at very high accretion rate (Lii et al. 2011). These simulations can possibly explain the FU Ori winds as discussed by Königl et al. (2011). We have not seen formation of fast outflows in current simulations of accretion in the BL regime. Recently, we were able to obtain outflows from stars rotating in the ‘propeller’ regime (Ustyugova et al. 2011). However, this is the case of the dynamically important field.

An interesting phenomenon of magnetospheric accretion through interchange instability observed in modelling of  $\alpha$ -discs (e.g., Romanova et al. 2008; Kulkarni & Romanova 2008), has not been observed in current simulations. We suggest that our simulations of magnetospheric accretion were not long enough to observe this instability, and/or the instability criterion can be somewhat different for cases of turbulent and  $\alpha$ -type discs.

## ACKNOWLEDGMENTS

Resources supporting this work were provided by the NASA High-End Computing (HEC) Program through the NASA Advanced Supercomputing (NAS) Division at Ames Research Center and the NASA Center for Computational Sciences (NCCS) at Goddard Space Flight Center. The research was supported by NASA grants NNX10AF63G, NNX11AF33G and NSF grant AST-1008636. AVK and GVV were supported in part by RFBR grants 09-01-00640a and 09-02-00502a.

## REFERENCES

- Armitage, P., 1998, ApJ, 501, L189
- Armitage, P., 2002, ApJ, 330, 895
- Arons, J., & Lea, S.M., 1980, ApJ, 235, 1016
- Bachetti, M., Romanova, M.M., Kulkarni, A., Burderi, L., di Salvo, T., 2010, MNRAS, 403, 1193
- Balbus, S.A., & Hawley, J.F. 1991, ApJ, 376, 214
- Balbus, S.A., & Hawley, J.F. 1998, Reviews of Modern Physics, Volume 70, 1

<sup>14</sup> In the opposite case of multiple turbulent cells in the disc (not considered here), the number of cells will accrete simultaneously and the funnel streams will be more symmetric.

- Beckwith, K., Hawley, J.F., & Krolik, J.H. 2009, *ApJ*, 707, 428
- Beckwith, K., Armitage, P.J., Simon, J.B. 2011, *MNRAS*, in press, (arXiv:1105.1789)
- Bessolaz N., Zanni C., Ferreira J., Keppens R., Bouvier J., 2008, *A&A*, 478, 155
- Bouvier, J., Alencar, S.H.P., Harries, T.J., Johns-Krull, C.M., Romanova, M.M. 2007, in: B. Reipurth, D. Jewitt, and K. Keil (eds.), *Protostars and Planets V*, University of Arizona Press, Tucson, vol. 951, p. 479
- Brandenburg, A., Nordlund, A., Stein, R. F., Torkelsson, U. 1995, *ApJ*, 446, 741
- Campbell, C.G. 2010, *MNRAS*, 403, 1339
- Chandrasekhar, S. 1960, *Proc. Nat. Acad. Sci.*, 46, 253
- Collier Cameron, A., Campbell, C.G. 1993, *A&A*, 274, 309
- Cumming, A., Zweibel, E., & Bildsten, L. 2001, *ApJ*, 557, 958
- D'Angelo, C. R., Spruit, H. C. 2010, *MNRAS*, 406, 1208
- Fisker J. L., Balsara D. S., 2005, *ApJ*, 635, L69
- Flock, M., Dzyurkevich, N., Klahr, H., Turner, N. J., Henning, Th. 2011, *ApJ*, in press, (arXiv:1104.4565) L75
- Ghosh, P., Lamb, F.K. 1979, *ApJ*, 232, 259
- Goodson, A.P., Winglee, R. M., & Böhm, K.-H. 1997, *ApJ*, 489, 199
- Goodson, A.P., Böhm, K.-H., Winglee, R. M. 1999, *ApJ*, 524, 142
- Hawley, J.F., Gammie, C.F., Balbus, S.A. 1995, *ApJ*, 440, 742
- Hawley, J.F., 2000, *ApJ*, 528, 462
- Hawley, J.F., Balbus, S.A., & Stone, J.M. 2001, *ApJ Letters*, 554, L49
- Hawley, J.F., Balbus, S.A., 2002, *ApJ*, 573, 738
- Hellier, C. 2001, *Cataclysmic variable stars: how and why they vary*, Springer-Praxis books in astronomy and space sciences, Praxis Publishing Ltd, Chichester, UK
- Igumenshchev, I.V., 2008, *ApJ*, 677, 317
- Illarionov, A.F., & Sunyaev R. A., 1975, *A&A*, 39, 185
- Inogamov N. A., & Sunyaev R. A., 1999, *Astron. Lett.*, 25, 269
- Kaisig, M., Tajima, T., Lovelace R. V. E. 1992, *AJ*, 386, 83
- Koldoba A. V., Romanova M. M., Ustyugova G. V., Lovelace R. V. E. 2002, *ApJ*, 576, L53
- Koldoba A. V., Ustyugova G. V., Romanova M. M., Lovelace R. V. E. 2008, *MNRAS*, 388, 357
- Königl, A. 1991, *ApJ*, 370, L39
- Königl, A., Romanova, M.M., Lovelace, R.V.E. 2011, *MNRAS*, 416, 757
- Kulkarni A. K., Romanova M. M. 2005, *ApJ*, 633, 349
- Kulkarni A. K., Romanova M. M. 2008, *ApJ*, 386, 673
- Kulkarni A. K., Romanova M. M. 2009, *ApJ*, 398, 701
- Lamb F. K., Pethick C. J., Pines D., 1973, *ApJ*, 184, 271
- Li, L.-X., & Narayan, R. 2004, *ApJ*, 601, 414
- Lii, P., Romanova, M.M., Lovelace, R.V.E. 2011, *MNRAS*, submitted, arXiv:1104.4374
- Lewin, W. H. G., van Paradijs, J., van den Heuvel, E. P. J. 1995, *X-Ray Binaries*, *Camb. Astropys. Ser.*, Vol. 26
- Long M., Romanova M. M., Lovelace R. V. E., 2005, *ApJ*, 634, 1214
- . 2007, *MNRAS*, 374, 436
- . 2008, *MNRAS*, 386, 1274
- Long M., Romanova M.M., Lamb F.K., 2011, *New Astronomy*, in press, (arxiv:0911:5455)
- Lovelace R. V. E., Romanova, M.M., Bisnovatyi-Kogan, G.S. 1995, *MNRAS*, 275, 244
- Lovelace R. V. E., Romanova, M.M., Bisnovatyi-Kogan, G.S. 1999, *ApJ*, 514, 368
- Lovelace R.V.E., Romanova, M.M., Newman, W.J. 2010, *MNRAS*, 402, 2575
- Lubow, S.H., & Spruit, H.C. 1995, *ApJ*, 445, 337
- Lynden-Bell D. 1996, *MNRAS*, 279, 389
- Miller, K.A., & Stone, J.M. 1997, *ApJ*, 489, 890
- Miller, K.A., & Stone, J.M. 2000, *ApJ*, 534, 398
- Mohanty, S., Jayawardhana, R. & Basri, G. 2005, *ApJ*, 626, 498
- Narayan, R., Igumenshchev, I. V., Abramowicz, M. A. 2003, *PASJ*, 55, L69
- Paczyński B., 1978, in Zytkov A., ed., *Nonstationary Evolution of Close Binaries*. Polish Scientific Publishers, Warsaw, p. 89
- Piro A. L., Bildsten L., 2004, *ApJ*, 610, 977
- Popham R., Narayan R., 1995, *ApJ*, 442, 337
- Pretorius, M. L., Warner, B., Woudt, P. A., 2006, *MNRAS*, 368, 361
- Pringle, J.E. 1989, *MNRAS*, 236, 107
- Pringle, J.E., Rees, M.J. 1972, *A&A*, 21, 1P
- Romanova M. M., Kulkarni A. K., Lovelace R. V. E., 2008, *ApJ*, 673, L171
- Romanova M.M., Long M., Lamb F.K., Kulkarni A.K., Donati J.-F. 2010, *MNRAS*, in press (arXiv:0912.1681)
- Romanova M. M., Lovelace R. V. E., 2006, *ApJ*, 645, L73
- Romanova M. M., Ustyugova G. V., Koldoba A. V., Lovelace R. V. E., 2002, *ApJ*, 578, 420
- . 2004, *ApJ*, 610, 920
- . 2005, *ApJ Letters*, 635, L165
- . 2009, *MNRAS*, 399, 1802
- . 2011a, *MNRAS*, 411, 915
- . 2011b, *MNRAS*, in prep
- Romanova M. M., Ustyugova G. V., Koldoba A. V., Wick J. V., Lovelace R. V. E., 2003, *ApJ*, 595, 1009
- Ronchi, C., Iacono, R., & Paolucci, P.S. 1996, *J. Comp. Phys.* 124, 93
- Shakura, N.I., & Sunyaev, R.A. 1973, *A&A*, 24, 337
- Shu, F.H., Lizano, S., Ruden, S.P., & Najita, J. 1988, *ApJ*, 328, L19
- Simon, J.B., Hawley, J.F., & Beckwith, K. 2011, *ApJ*, 730, 94
- Spruit, H.C., & Taam, R.E. 1990, *A&A*, 229, 475
- Spruit, H.C., Stehle, R. & Papaloizou, J.C.B., 1995, *MNRAS*, 275, 1223
- Steinacker, A., & Papaloizou, J.C.B., 2002, *ApJ*, 571, 413
- Stone, J.M., Hawley, J.F., Balbus, S.A., Gammie, C.F. 1996, *ApJ*, 463, 656
- Stone, J.M., & Pringle, J.E. 2001, *MNRAS*, 322, 461
- Tanaka, T. 1994, *J. Comp. Phys.*, 111, 381
- Ustyugova, G. V., Koldoba, A. V., Romanova, M. M., Lovelace, R. V. E., 2006, *ApJ*, 646, 304
- Van der Klis, M. 2000, *Ann. Rev. Astron. Astrophys.*, 38, 717
- Velikhov, E.P. 1959, *Soviet Physics*, - *JETP*, 36, 1398
- Wang, Y.-M. 1995, *ApJ Letters*, 449, L153
- Warner, B. 2003, *Cataclysmic Variable Stars*, *Cambridge Astrophysics Series*, vol. 28, Cambridge University Press
- Warner, B., Woudt, P. A., 2002, *MNRAS*, 335, 84